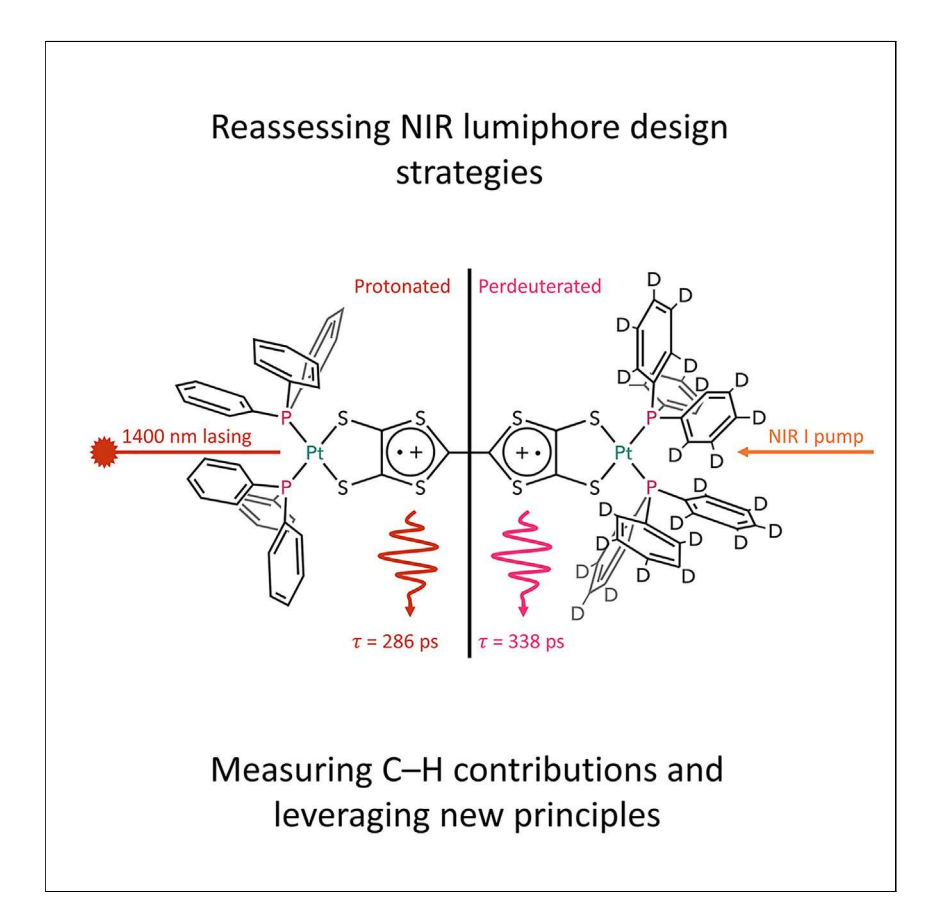
Chem



Article

Elucidating non-radiative decay in nearinfrared lumiphores: Leveraging new design principles to develop a telecom band organic dye laser



NIR emitters are employed in bioimaging, communication, and optics applications due to their emission in low-attenuation regions; however, they often exhibit low quantum yields, which is typically attributed to C–H modes. Here, we report perdeuteration of a NIR lumiphore, allowing us to assess C–H contributions for the first time. Our results indicate that C–Hs are not primary contributors to non-radiative decay, and we instead demonstrate the benefits of heteroatom substitution to red-shift emission while retaining brightness.



Lauren E. McNamara, Christopher Melnychuk, Jan-Niklas Boyn, Sophie W. Anferov, David A. Mazziotti, Richard D. Schaller, John S. Anderson

schaller@anl.gov (R.D.S.) jsanderson@uchicago.edu (J.S.A.)

Highlights

Perdeuteration of a deep NIR lumiphore allows for assessment of C–H contributions

C–H modes do not contribute significantly to non-radiative decay in the NIR region

Skeletal modes may play a larger role in low quantum yields for organic emitters

Heteroatom substitution enables reddest organic-based laser to date

McNamara et al., Chem 10, 2266–2282 July 11, 2024 © 2024 Elsevier Inc. All rights

https://doi.org/10.1016/j.chempr.2024.03.023







Article

Elucidating non-radiative decay in near-infrared lumiphores: Leveraging new design principles to develop a telecom band organic dye laser

Lauren E. McNamara,¹ Christopher Melnychuk,¹ Jan-Niklas Boyn,² Sophie W. Anferov,¹ David A. Mazziotti,¹ Richard D. Schaller,^{3,4,*} and John S. Anderson^{1,5,*}

SUMMARY

Organic near-infrared (NIR) lumiphores have been targeted for biological and technological applications; however, these dyes exhibit exponentially decreasing quantum yields with decreasing energy gaps. The accepted model of this phenomenon invokes C-H stretching modes as the dominant route of non-radiative energy dissipation. Reducing the number of these modes is a popular strategy for the design of bright NIR lumiphores, but quantitative experimental validation of this strategy is lacking. Here, we evaluate the role of C-H modes in non-radiative relaxation through isotopic labeling of a NIR-emitting complex. Measurements comparing relaxation between protonated and perdeuterated complexes indicate that C-H modes do not contribute significantly to non-radiative relaxation. We instead propose that skeletal modes may play a larger role and suggest that minimizing scaffold size is a promising route for bright NIR lumiphores. We demonstrate the promise of such strategies through the development of the reddest organicbased laser dye yet reported.

INTRODUCTION

NIR (700–1,700 nm) lumiphores are promising candidates for several applications. ^{1–9} These include biological imaging, as NIR emission falls into the tissue transparent range, ^{1–6} as well as in technological areas such as deep NIR (>1,200 nm) emitters that can also be used in the low-attenuation telecom bands (~1,260–1,550 nm). ^{1,10} Organic NIR dyes have been specifically targeted due to their biocompatibility (i.e., excretion); however, large conjugated systems are typically required to shift organic emission into the NIR region, and these dyes often suffer from low photoluminescence (PL) quantum yields (PLQYs). ^{1–6,11–14} Furthermore, PLQYs decrease roughly exponentially with decreasing emission energy, an empirical observation known as the energy gap law. ¹⁵ Thus, understanding the fundamental photophysical limitations on PLQY in the NIR region is vital to the design of improved lumiphores.

The dominant theoretical explanation for the energy gap law was proposed by Englman and Jortner (EJ) in 1970.¹⁵ Starting in the 1950s, it was hypothesized that non-radiative relaxation occurs by nonadiabatic coupling between ground and excited electronic states involving "promoting" vibrational modes, followed by rapid relaxation within the ground electronic state via energy dissipation into "accepting" vibrational modes. ^{16–21} EJ built upon these earlier works to derive a simple equation for the overall relaxation rate through a series of approximations involving the accepting modes. The EJ model emphasizes the role of the highest-frequency

THE BIGGER PICTURE

Near-infrared (NIR, 700-1,700 nm) lumiphores are promising for applications ranging from bioimaging to lowattenuation communication; however, most NIR emitters suffer from low quantum yields that drop off exponentially into the NIR region. For the past 50 years, this behavior has been attributed to C-H vibrational modes, which are present at the core of most organic NIR emitters. Thus, typical design strategies for bright NIR lumiphores include minimization of C-Hs. Here, we report full deuteration of an organic-based NIR emitter to assess the contributions of C-Hs to nonradiative decay. Our results suggest that C-Hs are not the primary driver of low quantum yields in the NIR region and instead suggest that skeletal modes may be more important. Lastly, we propose an alternate design strategy employing heavy heteroatom substitution to shift emission further into the NIR region while minimizing skeletal modes, allowing us to realize the reddest organic-based laser to date.







vibrations as accepting modes due to the need for an elevated vibrational level of the ground electronic state to be degenerate with the thermalized excited electronic state, and the approximate exponential decrease of Franck-Condon factors with increasing vibrational quantum number. The second consideration is responsible for the gap law behavior in the EJ model and C–H stretches, commonly the highest-frequency vibrations in organic molecules, are therefore widely assumed to mediate non-radiative relaxation.

Although the EJ model captures the overall exponential dependence of non-radiative relaxation on the energy gap observed experimentally, quantitative application of the EJ model requires proper identification of the promoting modes, accurate determination of nonadiabatic couplings, and a detailed understanding of the reorganization energy associated with energy dissipation into the accepting modes. ^{15–27} These quantities are difficult to accurately measure or calculate, limiting the utility of the EJ model as a framework for the rational design of NIR lumiphores. Fundamentally, the generic problem of vibration-mediated non-radiative relaxation and gap law behavior remains a topic of debate in chemistry, condensed matter physics, and materials science. ^{17,27–35} Several distinct physical models produce gap law-type behavior utilizing different assumptions or frameworks, ^{27,31–36} but only the EJ model has received appreciable investigation in molecules. The generic problem of vibration-mediated electronic relaxation is therefore of broad practical and theoretical interest.

One elegant experimental approach to evaluate the EJ model is isotopic substitution (deuteration) of C–H bonds. The EJ model predicts that the lower vibrational frequency of C–D bonds should substantially reduce non-radiative relaxation by increasing the number of vibrational quanta required to reach degeneracy. There have been several prior examples of deuteration of the ligand environment of transition metal lumiphores; however, these complexes primarily emit in higher energy regions where isotope effects are expected to be less prominent, and/or some may be better approximated by the strong-coupling regime. ^{22,37–40}

Furthermore, perdeuteration of large organic NIR lumiphores is generally difficult due to their structural and synthetic complexity. These compounds also often oxidize easily, limiting their applications and complicating spectroscopic experiments. ^{22,41} In limited examples of NIR organic lumiphores with partially deuterated cores, only minimal improvements in PLQY and non-radiative decay rates are observed. ^{42–44} These slight improvements contrast with those predicted by the EJ model in their respective spectral regions and thus raise questions about the quantitative utility of this model.

Our lab recently reported a compact, tunable scaffold that emits in the NIR II region (1,000–1,700 nm). These tetrathiafulvalene-2,3,6,7-tetrathiolate-based (TTFtt) complexes absorb and emit from a core free of C–Hs. These are typical organic $\pi-\pi$ transitions, making TTFtt an ideal platform for a broadly-applicable photophysical study. Prior work indicated that these TTFtt systems display large PLQYs and non-radiative lifetimes for the NIR II region, but which are still much lower than those of bluer-emitting compounds, in accordance with the broader gap law trend. Although these results imply that C–H vibrational modes are not major contributors to non-radiative decay rates, the presence of peripheral ligand-based C–H bonds prevented more definitive conclusions.

To further test the validity of the EJ model, we designed a series of proteo and perdeutero TTFtt isotopologs and evaluated the effects of ligand and solvent C-H

 $^{^{1}\}mbox{Department}$ of Chemistry, The University of Chicago, Chicago, IL 60637, USA

²Department of Mechanical and Aerospace Engineering, Princeton University, Princeton, NJ 08544, USA

³Center for Nanoscale Materials, Argonne National Laboratory, Argonne, IL 60439, USA

⁴Department of Chemistry, Northwestern University, Evanston, IL 60208, USA

⁵Lead contact

^{*}Correspondence: schaller@anl.gov (R.D.S.), jsanderson@uchicago.edu (J.S.A.) https://doi.org/10.1016/j.chempr.2024.03.023





modes on PLQYs and non-radiative lifetimes. We find only minimal changes in PLQY and non-radiative decay upon complete deuteration of peripheral ligands and/or solvent, providing convincing experimental evidence that C-H modes do not play a dominant role in these systems' non-radiative decay. Instead, skeletal ring vibrations may play a more dominant role in mediating relaxation. Our results place physical constraints on the parameters in an EJ-type analysis, and we find that the EJ model is inconsistent with our data when reasonable molecular parameters are used. This suggests that the minimization of C-Hs may not be a broadly useful strategy for designing bright NIR lumiphores and calls for a better theoretical framework to understand infrared non-radiative relaxation.

Fundamentally, these results, and other recent literature findings, demonstrate that alternative pathways should be considered when designing bright NIR lumiphores. One strategy to alter skeletal modes is through heteroatom substitution.⁴⁷ This allows for deep NIR emission to be centered on a much smaller scaffold than traditional NIR molecular dyes. This smaller scaffold size inherently reduces the number vibrations, which in turn should slow non-radiative relaxation. Indeed, TTFtt represents such a moiety, and we conclude this work by showing how the comparatively slow non-radiative decay in this molecule allows for the development of the reddest organic dye laser to date, with a lower threshold than current leading NIR organic laser dyes.

These findings motivate a revision of the fundamental photophysical limitations of deep NIR lumiphores and illustrate how compact heteroatom-substituted luminescent cores position chemical synthesis to push the boundaries of organic NIR emitters.

RESULTS

Synthesis and structure

We synthesized Pt(PPh₃)₂Cl₂ and its perdeuterated analog according to literature procedures, with either triphenylphosphine or triphenylphosphine-d₁₅. 48 While a synthetic route has been reported for {Pt(PPh₃)₂}₂TTFtt, we followed an alternate route from our lab using a $(SnBu_2)_2TTFtt$ precursor. ^{49,50} Subsequent oxidation with two equivalents of $[Fc^{BzO}][BAr^{F_4}]$ (where Fc^{BzO} = benzoylferrocenium and BAr^{F_4} = tetrakis(3,5-bis(trifluoromethyl)phenyl)borate, see Figure 1A) provides the dicationic analogs [{(PPh₃)₂Pt}₂TTFtt][BAr^F₄]₂ (1) and [{(PPh₃- d_{15})₂Pt}₂TTFtt][BAr^F₄]₂ (1- d_{60}).

Single-crystal X-ray diffraction reveals an analogous structure to previously reported TTFtt complexes of Pt (Figure 1B). The central C3-C4 distances range from 1.402 to 1.407 Å across both 1 and 1- d_{60} . Theory suggests this distance correlates with the diradical character in TTFtt.⁵¹ The distances shown here are relatively longer compared with those of other analogs, suggesting moderate diradical character in the solid state. This diradical character is confirmed via a solution-phase magnetic moment of 2.45 μ_B measured via Evans method (see Figure S7).

Room temperature photophysical characterization: The role of intersystem crossing

The room temperature photophysical properties of both analogs were characterized in dichloromethane (CH₂Cl₂) and dichloromethane-d₂ (CD₂Cl₂, Table 1). UV-vis-NIR spectra show intense (\sim 107,000 M⁻¹cm⁻¹) π - π transitions at 1,100 nm, which are redshifted compared with previously reported analogs.⁴⁵ These complexes emit in the deep NIR II region, at 1,266 nm (Figure 1C). The PLQY of 1 in CH₂Cl₂ is 0.070%. Although this PLQY is notably high for deep NIR emission, it is still quite low compared with blueremitting lumiphores and consistent with the broader gap law trend.⁴⁶



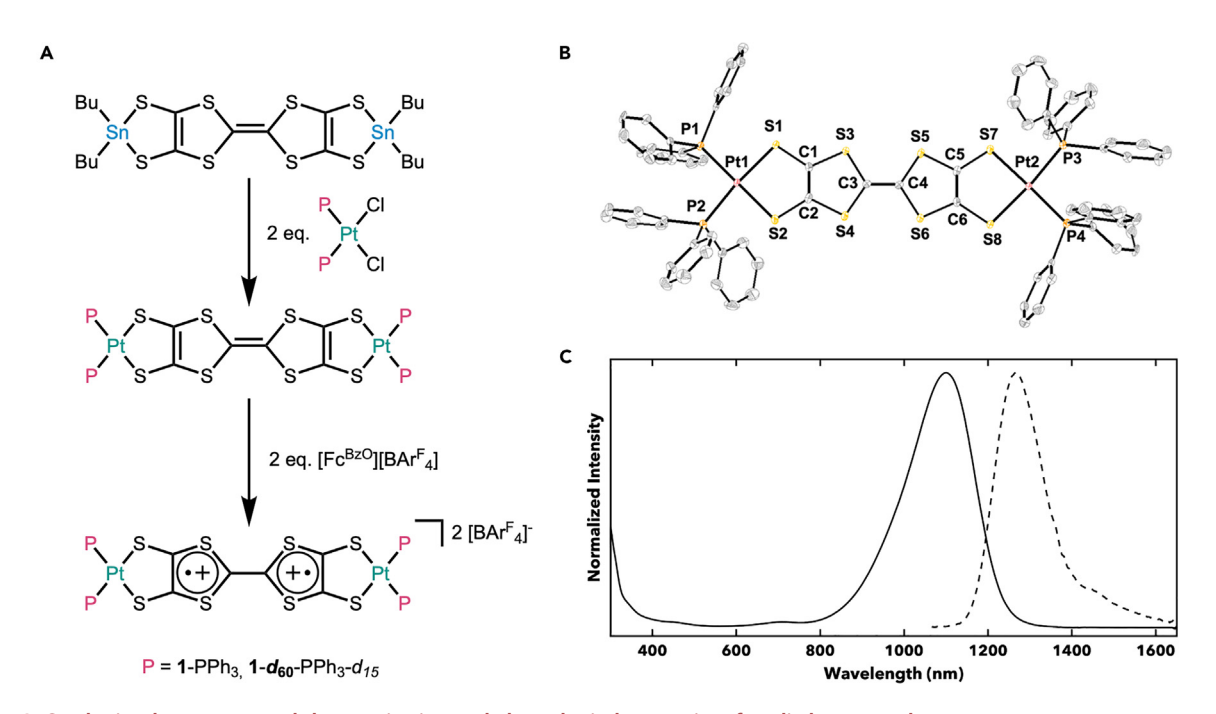


Figure 1. Synthetic scheme, structural characterization, and photophysical properties of studied compounds

(A) Synthesis of 1 and 1- d_{60} . See supplemental information and experimental procedures for synthetic details.

(B) Single-crystal X-ray structure of 1.

(C) Absorption (solid) and emission (dashed) spectra of 1 in CH_2Cl_2 .

Dicationic $1-d_{60}$ contains no C–Hs, providing a straightforward test of these moieties' involvement in non-radiative decay. The PLQY data in CD₂Cl₂ provide a further control for possible relaxation mediated by solvent C–Hs. Deuteration of peripheral ligands only marginally improves the PLQY to 0.083% for $1-d_{60}$ in CH₂Cl₂. Solvent deuteration also has only a minimal effect on PLQY, raising it to 0.077% for 1 in CD₂Cl₂. Perdeuteration of both solvent and ligands results in the largest overall improvement, albeit still small, with a PLQY of 0.108% for $1-d_{60}$ in CD₂Cl₂. Such a small impact demonstrates that C–H modes are not the primary non-radiative decay pathway in these systems at room temperature.

We then conducted picosecond transient absorption (TA) measurements to further clarify the role of deuteration on non-radiative decay and assess alternative non-radiative decay pathways (Figure 2). The overall TA spectra at early timepoints

Table 1. Photophysical parameters of various analogs		
	1	1-d ₆₀
ФСН2СІ2	0.00070	0.00083
ΨCD2Cl2	0.00077	0.00108
τ _{CH2Cl2} (ps) ^a	34.5 ± 7.4	33.9 ± 6.1
$ au_{CD2Cl2}$ (ps) ^a	42.0 ± 6.4	42.33 ± 7.3
$k_{nr,CH2Cl2} (s^{-1})^a$	2.90×10^{10}	2.95×10^{10}
$k_{nr,CD2Cl2} (s^{-1})^a$	2.38×10^{10}	2.36×10^{10}
τ _{CH2Cl2} (ps) ^b	286.33	338.74
τ _{CD2Cl2} (ps) ^b	388.84	570.00

See experimental procedures and supplemental information for details and equations used in determination of quantum yields, rates, and lifetimes.

^aData acquired at 298 K by TA.

^bData acquired at 10 K by TCSPC.





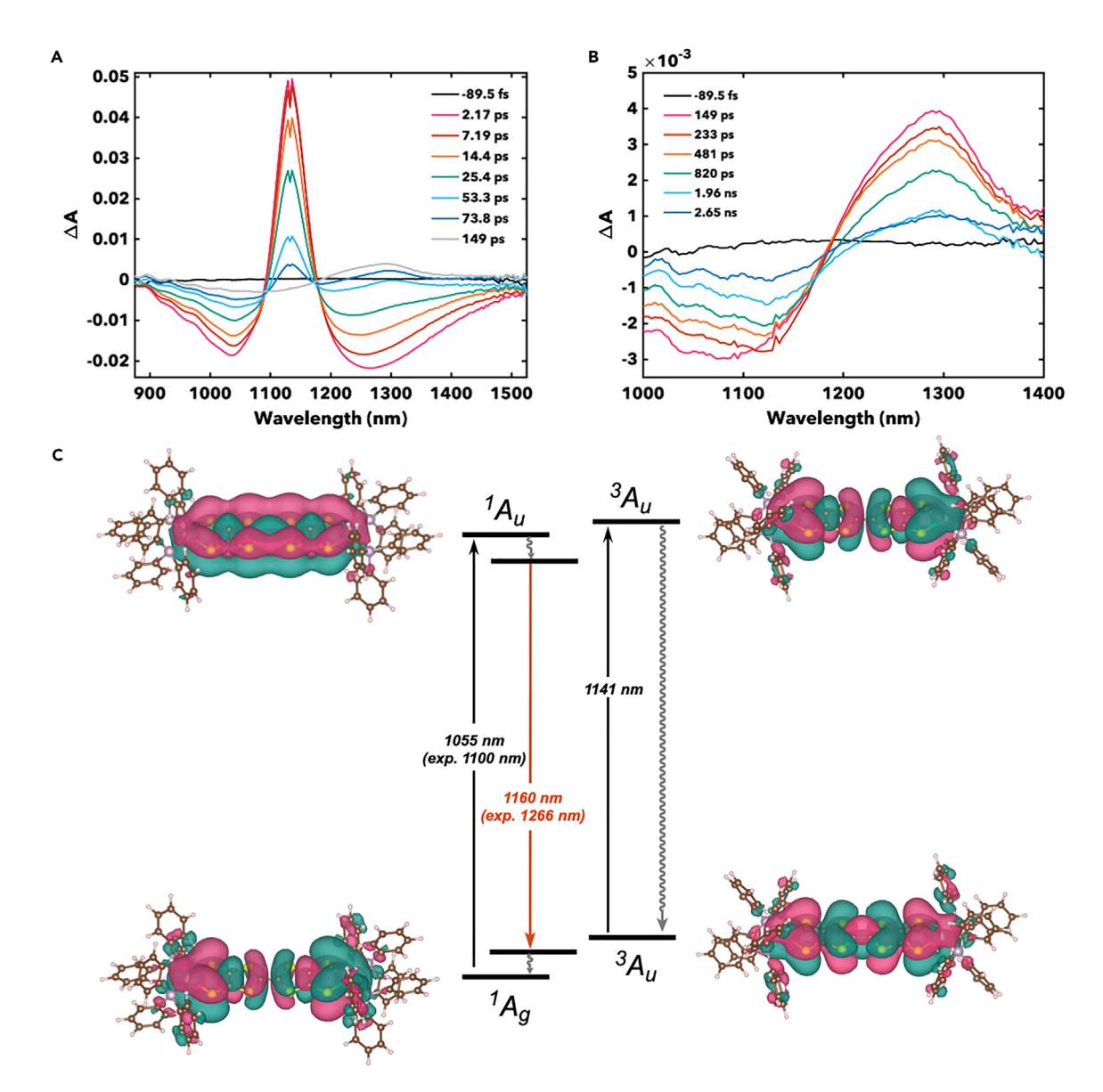


Figure 2. Electronic structure of studied dictations

- (A) Transient absorption spectra of $1-d_{60}$ at early time points.
- (B) Transient absorption spectra of $1-d_{60}$ at later time points.
- (C) Electronic structure of 1. 1 Au corresponds to S_{1} and upper 3 Au corresponds to T_{2} . All spectra acquired in CD₂Cl₂ at 298 K.

(<149 ps) show population and decay of a previously-assigned first singlet excited state in these complexes (S_1 , Figure 2A).⁴⁵ The spectra show a characteristic ground-state bleach (GSB) around 1,050 nm, an excited state absorption (ESA) at \sim 1,130 nm, and stimulated emission (SE) at 1,260 nm. Importantly, the position of each feature does not substantially shift with deuteration of ligands and/or solvent, suggesting that deuteration has little to no effect on the excited state energetics of these complexes (see supplemental information).

The S_1 spectrum decays fully by \sim 125 ps with concurrent formation of a new feature which we assign as a separate excited state (Figure 2B). Notably, this new excited state still shows a GSB in the same region as the NIR absorption peak for both compounds, as well as a new ESA around 1,290 nm. The weak signal and the density





functional theory (DFT)-predicted proximity of a triplet excited state (T_2) to S_1 (1.026 kcal/mol, Figure 2C and supplemental information) suggests that these new features correspond to the thermal population of T_2 by ISC. While ISC between singlet and triplet states of the same configuration (such as $^1\pi\pi^*$ to $^3\pi\pi^*$) is typically symmetry forbidden according to El-Sayed's rule, this TTFtt core can be modeled using C_i symmetry, which, along with molecules belonging to $C_{\rm nh}$ point groups, allows for spin-orbit coupling (SOC) between states of the same configuration. 52,53

The relatively fast ISC observed here is expected in organic systems with heavy atoms and illustrates another non-radiative decay route for lumiphores with heavy heteroatom substitution. Prior work on these systems established that the lifetime of S_1 extracted from TA is identical to the PL lifetime governing the PLQY, so we used the S_1 TA decay of proteo and deutero isomers to evaluate whether C–H modes impart any significant effect on the S_1 lifetime at room temperature. The lifetime data are broadly consistent with the PLQYs; the lifetimes of 1 and 1- d_{60} are identical within error (Table 1), while solvent deuteration lengthens the lifetime by about 30%. This indicates that C–H modes do not play a major role in the room temperature non-radiative relaxation of S_1 .

Variable temperature photophysical measurements: The role of vibrations

To more directly examine the role of vibrations in non-radiative relaxation of S_1 , we reduced ISC as a competing pathway by cooling to eliminate thermal population of the energetically proximal triplet. Steady-state and time-resolved variable temperature (VT) measurements on 1 and 1- d_{60} are consistent with small S_1 - T_2 gaps of about 400 cm⁻¹ for both analogs based on a simple Boltzmann model, with T_2 being higher-lying. Measurements were conducted in both polymer (poly(butyl methacrylate-co-isobutyl methacrylate), see experimental procedures and supplemental information) and a glassing solvent mixture (1:1 CH₂Cl₂:toluene or 1:1 CD₂Cl₂:toluene-d₈) to assess possible rigidification effects associated with solvent freezing. As shown in Figures 3A and 3B, lifetimes saturate below 100 K in all cases, indicating that the proposed ISC pathway is eliminated below this temperature. In this regime, where we expect a vibration-mediated mechanism to dominate, the largest deviation in lifetimes upon deuteration arises between 1 in 1:1 CH_2Cl_2 :toluene and $1-d_{60}$ in 1:1 CD_2Cl_2 :toluene- d_8 ; however, there is less than a 2-fold improvement upon deuteration of both solvent and ligand. As shown in Figure 5 and further discussed in subsequent sections, these results are inconsistent with the EJ model even at a qualitative level.

The VT time-correlated single photon counting (TCSPC) data also agree well with the VT PL data, with minor deviations in the PL data likely arising from changes in ground-state population between S_0 and T_1 (Figures 3C and 3D). The low-temperature PL data show vibronic features, spaced roughly $\sim 350~\rm cm^{-1}$ apart, which have been previously assigned in related group 10 dithiolene systems as out of phase deformations of the five-membered rings (see Figures 3C and S42). ⁵⁴ In most molecular and polymeric organic lumiphores, analogous vibronic structure is attributed to skeletal or C–H bending modes in the 1,000–1,500 cm⁻¹ region, and, from an photophysical standpoint, the combination of coupling strength and selection rules clearly favors non-C–H stretching modes in a diverse range of molecules. ^{1,22} As discussed below, we tentatively propose that such modes may be important in non-radiative relaxation.

We emphasize that because PLQYs and lifetimes remain small even below 100 K and upon complete deuteration, there must be major non-radiative pathways that are





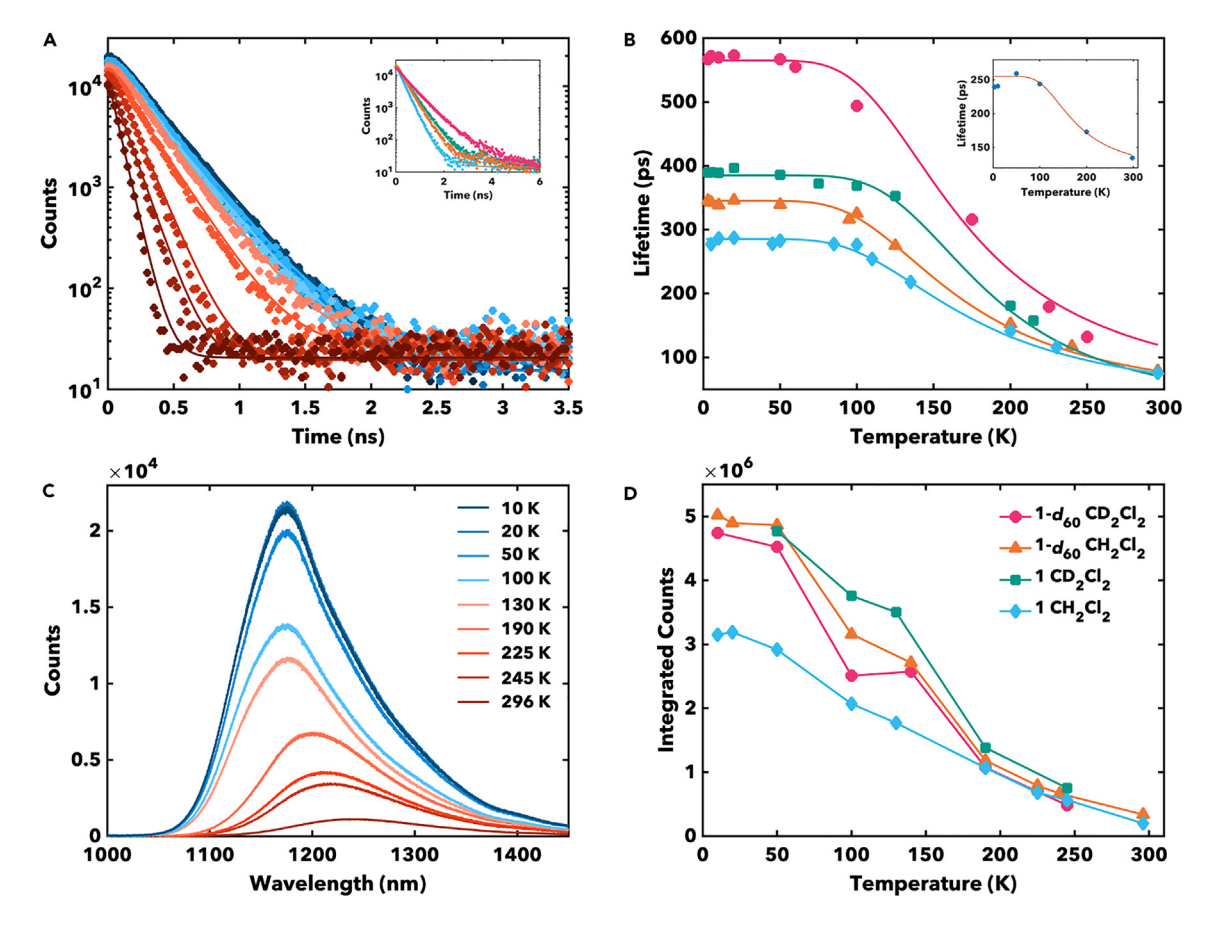


Figure 3. Shutting off intersystem crossing at low temperature

- (A) Time-resolved PL spectra for 1 in 1:1 CH_2Cl_2 : toluene from 296 to 5 K. Inset: overlaid 5 K time-resolved PL for 1 and 1- d_{60} , in 1:1 CH_2Cl_2 : toluene and 1:1 CD_2Cl_2 : toluene- d_8 .
- (B) Variable temperature lifetimes of 1 and $1-d_{60}$ in 1:1 CH₂Cl₂:toluene and 1:1 CD₂Cl₂:toluene- d_8 fit to a Boltzmann distribution. Inset: variable temperature lifetimes of 1 in polymer, fit to a Boltzmann distribution.
- (C) Variable temperature PL of 1 in 1:1 CH₂Cl₂:toluene.
- (D) Variable temperature integrated counts for 1 and $1-d_{60}$, in 1:1 CH₂Cl₂:toluene and 1:1 CD₂Cl₂:toluene- d_8 .

not related to C-H vibrations. Some possibilities include C-C skeletal vibrations, but further investigation will be needed to assign these decay mechanisms. Irrespective of the exact non-radiative decay pathway, C-H stretching modes do not meaningfully govern vibration-mediated non-radiative decay in the systems studied here, in direct contrast to common interpretations of the EJ model.

Vibrational structure

Given the coupling to lower-frequency modes implied by the low-temperature vibronic structure (see Figures 3C and S42), we investigated whether secondary effects of deuteration on nearby phenyl C=C modes might also be visible and potentially affect non-radiative relaxation. Indeed, the 10 K PL spectra show a subtle (6 nm, or $40~\rm cm^{-1}$, see Figure 4A) shift from 1 in CH₂Cl₂ to 1- d_{60} in CD₂Cl₂. This is the same shift observed in the infrared absorption spectra of 1 and 1- d_{60} in the region corresponding to conjugated C=C stretches (Figure 4B).

This shift is also supported by theory, which predicts a 41 cm⁻¹ shift of the outer phenyl C=C mode frequencies upon deuteration. Notably, these stretches are also predicted to couple with core TTF C=C stretches (see Figure 5C, supplemental



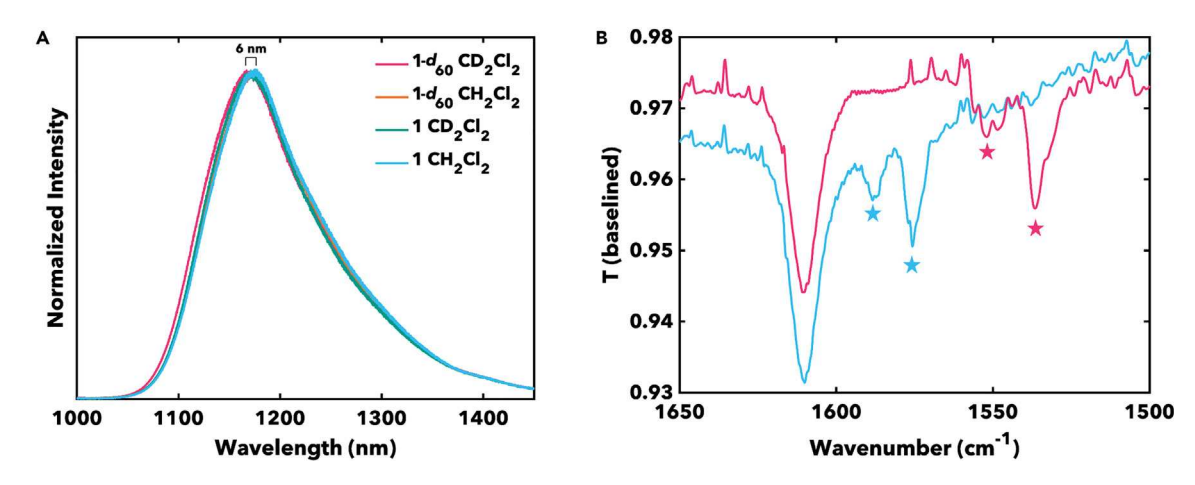


Figure 4. The observed shifts of skeletal vibrations upon deuteration (A) Overlayed 10 K PL spectra of 1 and $1-d_{60}$ in 1:1 CH₂Cl₂:toluene and 1:1 CD₂Cl₂:toluene- d_8 . (B) IR spectra of 1 (light blue) and $1-d_{60}$ (magenta) dropcast onto KBr windows.

information and Videos S1 and S2). 55-60 Such deuteration effects on skeletal mode frequencies have been observed in other systems, and it is well-known that skeletal modes can couple to excitations. 61,62 The close correspondence between these modes' frequency changes and the magnitude of the Stokes shift suggests that these modes may dominate the observed Stokes shift. Contribution of the accepting modes to the Stokes shift is a key parameter in the EJ model, and these lower frequency vibrations may therefore play this role in the non-radiative relaxation. Earlier work has indeed suggested a more prominent role of skeletal modes in non-radiative relaxation. 62,63

While these data suggest that the coupling to these low energy vibrations might contribute to non-radiative decay, these systems still have high PLQYs for this deep NIR region. 22,63 This is likely facilitated by the compact, rigid nature of the TTFtt scaffold where the emissive transition is centered. Although skeletal vibrations may contribute to non-radiative decay, all vibrations are ultimately minimized by the compact size of TTFtt, which allows for NIR II emission without extended conjugation. This is enabled by heteroatom substitution, which compresses the π system and redshifts the absorption and emission. 47 Calculations suggest that substitution with an even heavier heteroatom such as Se is predicted to shift absorption and emission further into the deep NIR II region (see Figure S51; Table S7) without adding additional vibrational modes. Heavier heteroatom substitution is therefore a promising area of future investigation.

Comparison with EJ model predictions

The version of the EJ model most widely used to interpret organic non-radiative decay is the following:

$$\frac{1}{\tau_{NR}} = \frac{J^2}{\hbar} \sqrt{\frac{2\pi}{\hbar\omega_M E}} \exp\left(-\left(\ln\left(\frac{E}{de_M}\right) - 1\right) \frac{E}{\hbar\omega_M}\right)$$
 (Equation 1)

where J is the matrix element for nonadiabatic coupling between excited and ground electronic potentials, ω_M is the angular frequency of the highest-frequency vibration in the system, E is the electronic energy gap, e_M is the nuclear reorganization energy associated with the highest-frequency mode, and d is the number of normal modes present at that frequency. The product de_M is the total contribution





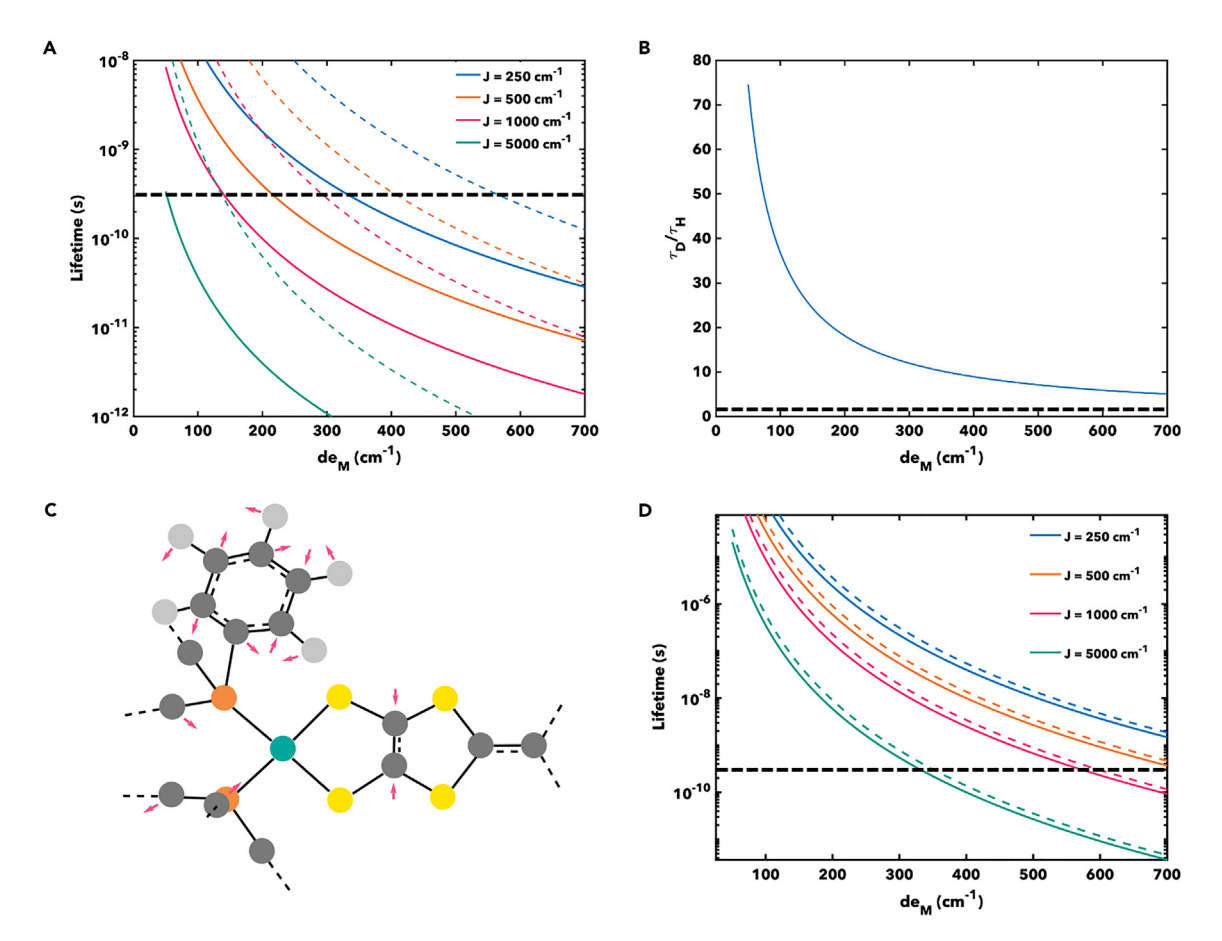


Figure 5. Energy gap law predictions and calculated vibrational shifts

(A) Comparison of predicted lifetimes given coupling to C–H (1, solid) and C–D (1- d_{60} , dashed) modes. Black dashed line marks the experimental low temperature lifetime (\sim 300 ps).

(B) Predicted lifetime ratio between protonated and deuterated molecules as a function of de_{M} . Black dashed line represents \sim 2-fold improvement seen experimentally.

(C) Linear combination of vibrations from simulations, corresponding to calculated 1,391 (1) and 1,350 (1- d_{60}) cm⁻¹ features. See Video S2 for full simulation.

(D) Comparisons of predicted lifetimes given dissipation through 1,580 cm $^{-1}$ (solid) and 1,540 cm $^{-1}$ (dashed) modes. Black dashed line marks the \sim 300 ps experimental lifetime.

of the highest-frequency modes to the Stokes shift and is constrained by experiment to be less than or equal to $700~{\rm cm}^{-1}$ in 1 and 1- d_{60} . The following calculations take E as 9,300 cm $^{-1}$, from the 10 K absorption and emission data for 1 in polymer.

To compare our low-temperature data with the EJ model, we took the experimental low-temperature lifetime of $\sim\!300$ ps for 1 as a comparative lifetime, depicted as a dashed black line in Figure 5A, and compared this value with those calculated from Equation 1 for C–H/D isotopologs. These calculated values are shown as colored solid and dashed lines, respectively, for different values of J. Assuming that 250 cm $^{-1}$ is a reasonable lower limit for J, the intersections between the 300 ps lifetime (black dashed line) and the solid C–H curves give an upper bound of about 350 cm $^{-1}$ on $de_{\rm M}$. This represents the amount of Stokes shift which would be attributable to C–H/D stretching modes. With $de_{\rm M} \leq 350$ cm $^{-1}$, Figure 5A indicates that non-radiative lifetimes in excess of several nanoseconds would be expected upon deuteration. The corresponding ratio of C–D to C–H lifetimes, which is independent of J, also predicts at least an order of magnitude increase in the





lifetime and PLQY (Figure 5B). Even in the hypothetical case where the *entire* Stokes shift is attributed to C–H/D stretch modes, a much stronger isotope effect is predicted by the EJ model than is observed. The large discrepancy between the predictions of the EJ analysis and our experiments further indicates that C–H modes are not the limiting factor in non-radiative decay.

Given the observed correlation between the C-D isotope effects on C=C modes and the measured Stokes shift, it is alternatively possible that C=C modes are a dominant contributor to non-radiative relaxation in our system. To test this hypothesis, we then performed a related analysis with the EJ model, but instead assuming that skeletal vibrations are the dominant accepting modes. The resulting lifetimes are shown in Figure 5D and qualitatively support our experimental observations. This analysis predicts a ~1.4-fold slowing of the non-radiative relaxation upon a shifting of the C=C frequency from 1,580 to 1,540 cm⁻¹ upon deuteration. This 1.4-fold slowing is indeed similar to the observed lifetime improvement upon deuteration of the molecule (1.4-fold in CD₂Cl₂ and 1.2-fold in CH₂Cl₂). Following previous arguments, however, the intersection of our experimental lifetime (dashed black line) with these predicted curves implies rather large values of de_M and/or J. Such large values may be discernable via simulations or spectroscopic experiments, ⁶² and this is a potential future area of investigation. The small yet distinct solvent effect indicates that intermolecular interactions also contribute to non-radiative relaxation, in contrast to the assumption that molecular non-radiative relaxation is purely intramolecular. 15

PLQYs are in general affected by multiple non-radiative processes in composite manner, and it is possible that a variety of heretofore-neglected pathways contribute to the total non-radiative relaxation. This suggests that designing a bright NIR molecule requires a more holistic consideration of molecular electronic and vibrational structure than minimizing C–H modes alone.

Demonstration of a 1,400 nm organic dye laser

Given the emission energy and lifetimes of 1, as well as the observation of an SE feature around 1,260 nm in the TA data, we investigated the performance of 1 as a deep NIR laser dye. Current progress in this area has led to organic dye lasers that can be tuned beyond 1,200 nm, but no candidates beyond 1,400 nm have been reported. $^{63-65}$

Complex 1 was placed in a 3 mm fluorescence cuvette and transversely stripe pumped by an 800 nm, 200 ps pulsewidth Ti:sapphire laser, without stirring or flowing. Light emission from the cavity was detected with a 0.3 m spectrograph and cooled InGaAs array. As a function of pump intensity, a distinct output threshold was reached around 1.68 mJ/mm², where the emission narrowed (the PL spectrum for 1 shows the emission full width at half maximum, FWHM, is \sim 200 nm, Figure 1C). A central peak consistent with lasing was observed at 1,371 nm, with a nearly equally intense shoulder around 1,400 nm (Figure 6A). The power conversion was measured to be 5.6%, consistent with other NIR lasers. Here features span the range from 1,300 to 1,500 nm, making 1 the reddest organic-based laser dye yet reported. This range is additionally of interest as it spans the telecom region, where attenuation is minimized.

Misalignment of the cavity results in a loss of signal intensity, and signal is recovered after realignment (Figure 6C). Complex 1 demonstrates reasonable photostability over \sim 20,000 laser shots without stirring or flowing, and the dye continued to lase with a moderate decrease in intensity (Figure 6D) putatively from degradation under illumination. Comparison with the commercially available NIR laser dye, IR 26,





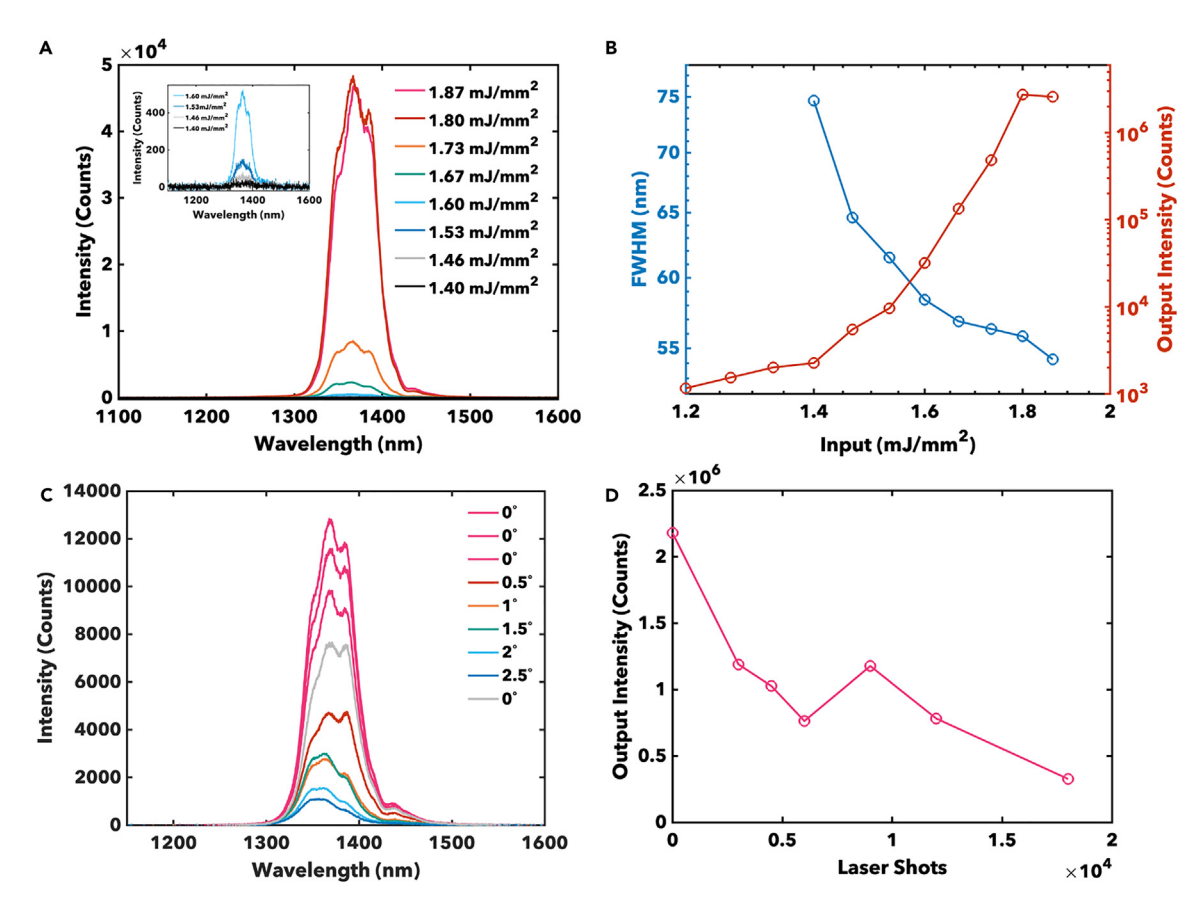


Figure 6. Demonstration of a telecom band laser

- (A) Laser profile of 1 in CH_2Cl_2 as a function of input power.
- (B) FWHM and integrated output intensity of ${\bf 1}$ in CH_2CI_2 as a function of input power.
- (C) Laser intensity and profile of 1 in CH_2Cl_2 given an input fluence of 1.87 mJ/mm², upon cavity destruction via turning the mirror knob. The gray trace is the return to the original position after cavity misalignment.
- (D) Photostability of 1 in CH_2Cl_2 under 1.87 mJ/mm^2 input fluence.

indicates 1 has a lower threshold, is significantly redshifted, and features a narrower FWHM (see Figure S48).^{63,64} We believe that these light emission improvements over IR 26 arise from the longer lifetime, facilitated by the compact nature of the TTFtt scaffold.

To further improve the threshold, we also investigated a previously reported TTFtt-based dye ([{(dppe)Pt}_2TTFtt][BAr $_4$ F] $_2$, 2, dppe = 1,2-bis(diphenylphosphino)ethane, see Figures S45 and S47) for lasing. ^{45,66} While not as red as 1, the reported lifetimes of 2 at room temperature are appreciably longer. Consequently, we see the threshold reduced to 1.46 mJ/mm 2 , while still lasing at longer wavelengths than IR 26 (see Figures S46 and S48). Additionally, 2 demonstrates the tunability of this system; upon modification of capping ligands, the resultant laser maximum can be significantly shifted. We note that additional tuning should be possible due to the strong solvatochromic behavior of these compounds ⁴⁵; different solvent dielectrics should shift these dyes further into desirable regions.

DISCUSSION

We have synthesized two new Pt-capped TTFtt analogs to investigate the role of C–H modes on non-radiative decay. Our data indicate that C–H modes do not impact





lifetimes as significantly as implied by the widely utilized EJ model. These results, along with recent literature findings, 40,42-44 challenge established design principles for deep NIR-emitting organic molecules and motivate the investigation of alternative design strategies for lumiphores in this region. Furthermore, these data should prompt renewed theoretical and computational investigations to form a more complete and quantitative picture for vibration-mediated non-radiative relaxation.

This work further suggests that compact, rigid scaffolds are a strategy to minimize the influence of any vibrational modes which may contribute to non-radiative decay. Heteroatom substitution allows for deep NIR emission without extended conjugation, optimizing lifetimes through compactness and rigidification. Such optimized lifetimes allow for the demonstration of a 1,400 nm organic-based laser dye. Ultimately, these design principles open the door for improved deep NIR-emitting organic lumiphores.

EXPERIMENTAL PROCEDURES

Resource availability

Lead contact

Further information and requests for resources should be directed to and will be fulfilled by the lead contact, John Anderson (jsanderson@uchicago.edu).

Materials availability

Compounds used in this study may be available from John Anderson (jsanderson@uchicago.edu) with a completed materials transfer agreement. Availability is subject to the current stocks in the laboratory.

Data and code availability

All data reported in this paper will be shared by the lead contact upon request.

General synthetic methods

All transmetalation and oxidation procedures were performed under inert conditions (dry N_2) in a MBraun UNIIab glovebox. Elemental analyses (C, H, and N) were conducted by Midwest Microlabs. All solvents used were dried and purged with N_2 on a pure process technology solvent system and subsequently filtered through activated alumina and stored over 4 Å molecular sieves. TTFtt(SnBu₂)₂, ⁵⁰ Pt(PPh₃)₂Cl₂, ⁴⁸ [Fc^{B2O}][BAr^F₄], ⁵⁰ and 2^{45} were prepared according to literature procedures. Pt(PPh₃- d_{15})₂Cl₂ was prepared according to a modified version of the Pt(PPh₃)₂Cl₂ procedure, using triphenylphosphine- d_{15} instead of triphenylphosphine. ⁴⁸ All other chemicals and reagents were purchased from commercial sources and used as received.

Single-crystal X-ray diffraction

All single-crystal X-ray diffraction data were collected at 100 K on a Bruker D8 VENTURE diffractometer equipped with a microfocus Mo-target X-ray tube (λ = 0.71073 Å) and a PHOTON 100 CMOS detector. Single crystals were mounted on a cryo-loop and transferred into the diffractometer nitrogen stream before collection. Data reduction and integration were performed with the Bruker APEX3⁶⁷ software package (Bruker AXS, version 2015.5-2, 2015). Data were scaled and corrected for absorption effects using the multi-scan procedure as implemented in SADABS (Bruker AXS, version 2014/54, 2015). All crystal structures were solved by SHELXT⁶⁸ (version 2014/55) and refined by a full-matrix least-squares procedure using OLEX26⁶⁹ (XL refinement program version 2018/17). Disorder was modeled with common restraints.





Cyclic voltammetry

Cyclic voltammetry measurements were performed using a glassy carbon working electrode, a silver wire pseudoreference, and a platinum wire counter electrode. Each voltammogram was referenced to an internal standard (Fc⁺/Fc). All measurements were acquired using a BASi Epsilon potentiostat and analyzed using the BASi Epsilon software version 1.40.67NT.

Fourier transform infrared spectroscopy

All IR measurements were performed by dropcasting CH_2CI_2/CD_2CI_2 solutions onto KBr plates. Each spectrum was acquired on a Bruker Tensor II; both background subtractions and baseline corrections were applied for each complex using the OPUS software.

NMR spectroscopy

¹H, ³¹P, and ¹⁹⁵Pt nuclear magnetic resonance (NMR) spectra were acquired on Bruker DRX 400 and 500 spectrometers. Residual solvent peaks were referenced for all ¹H NMR measurements, and 85% phosphoric acid and sodium hexachloroplatinate were used as references for ³¹P and ¹⁹⁵Pt NMR measurements, respectively. Evans method measurements were conducted in CD₃CN with a capillary insert of 95/5 w/w% CD₃CN/MeCN. Pascal's constants were used to correct for the diamagnetic contribution. ⁷⁰

UV-vis-NIR

UV-vis-NIR measurements were performed using a Shimadzu UV-3600 plus dual beam spectrophotometer.

PL spectroscopy

Room temperature emission spectra were acquired on a Horiba Scientific PTI QuantaMaster fluorometer. Low-temperature emission spectra were recorded by loading samples in 1:1 CH₂Cl₂:toluene or 1:1 CD₂Cl₂:toluene-d₈ into 0.5 mm cuvettes, sealing with vacuum grease, and cooling in a Janis cryostat.

TA spectroscopy

TA spectroscopy was performed using a 5 kHz amplified titanium:sapphire laser with a 120 fs laser pulse width. A portion of the 800 nm fundamental output was focused into a sapphire crystal to produce NIR continuum probe pulses that were mechanically delayed. Pump pulses were tuned to 950 nm using an optical parametric amplifier, and a mechanical chopper reduced the repetition rate to 2.5 kHz. Samples were stirred during experiments and excited with 0.2 mW of pump power.

Lifetime measurements

Time-correlated single photon counting was performed on the samples using a 975 nm diode laser with a 60 ps pulse width operating at 20 MHz. Collected PL was dispersed using a 0.3 m spectrograph and detected with a superconducting nanowire single photon detector and multichannel scaler with 25 ps bin width. Of note, the instrument response function (IRF) falls around \sim 60 ps. VT lifetimes were fit to a simple Boltzmann using the following equation:

$$B = \frac{1}{\frac{\Delta H}{1 + e^{\frac{T}{R}}} \left(\frac{1}{T} - \frac{1}{T_{1/2}}\right)}$$

and

$$\tau_{PL} = (B \times \tau_{HT}) + ((1 - B) \times \tau_{LT})$$





where τ_{HT} and τ_{LT} are the high and low temperature lifetimes.

PL quantum yield determination

The samples, sealed in NMR tubes, were individually placed in an integrating sphere (Thorlabs, IS200-4) with an PbSe detector (Thorlabs, PDA20H) on one port and directly excited by an 808 nm diode laser (Thorlabs, M9-808-0150) of 15 W/cm² average intensity under 1 kHz square-wave modulation. The detector signal *S*, with and without a silicon window on the detector port, was recorded with the sample and with a DCM blank. 808 nm light is completely blocked by the silicon window within the sensitivity of the measurement. The PL quantum yield is therefore the following:

$$\varphi = S_{S,Si} / T(S_D - S_S)$$

where the subscripts S, D, and Si, respectively, denote the sample, DCM blank, and silicon window. T is the total normalized emission signal transmitted by the silicon window. Due to the spectral overlap between the sample emission and the soft absorption edge of silicon, we calculate T explicitly as

$$\int E(\lambda) d\lambda \times \left(\int \frac{E(\lambda)}{T(\lambda)} d\lambda \right)^{-1}$$

where $E(\lambda)$ is the normalized sample emission spectrum and $T(\lambda)$ is the normalized silicon window transmission spectrum.

Non-radiative rate determination

The non-radiative and radiative rates were determined using the experimentally determined quantum yield values, φ , and the singlet TA lifetimes. Both values were utilized using the expression $\varphi = k_r/(k_r + k_{nr})$, where the denominator, $(k_r + k_{nr})$, is the reciprocal of the TA lifetime, τ .

Synthetic procedures

Synthesis of $[{(PPh_3)_2Pt}_2TTFtt][BAr^F_4]_2$ (1)

TTFtt(SnBu₂)₂ (0.050 g, 0.063 mmol) was dissolved in 4 mL of DCM and slowly added to a solution of Pt(PPh₃)₂Cl₂ (0.100 g, 0.126 mmol) in 3 mL of DCM. The colorless solution formed a shiny pink suspension upon addition of the orange solution of TTFtt(SnBu₂)₂ and was left to stir for 10 min. Next, [FcBzO][BArF4] (0.145 g, 0.126 mmol) was dissolved in 4 mL DCM and slowly added to the stirring reaction. The pink suspension turned brown and then olive green upon full addition of [Fc^{BzO}][BAr^F₄] and was left to stir 5 min. The solution was condensed to 1 mL under vacuum, and petroleum ether (5 mL) was slowly added. Green crystals immediately began to form. The solids were washed with petroleum ether several times (3 \times 5 mL) and dried under vacuum. The crude product was redissolved in 2 mL of DCM, filtered through celite, and layered with petroleum ether. The layered solution was cooled to -35° C and left to crystallize overnight. The resulting green crystals were collected and dried (0.219 g, 99% yield). Crystals suitable for diffraction were selected from a dichloromethane/petroleum ether slow diffusion gradient left to crystallize over a 2 days period at -35°C. ¹H NMR (500 MHz, CD₂Cl₂, 298 K): δ 7.23-7.27 (m, PPh₃), 7.36–7.43 (m, PPh₃), 7.55 (s, $[BAr^{F_4}]^{-}$), 7.73 (s, $[BAr^{F_4}]^{-}$). $^{31}P\{^{1}H\}$ NMR (162 MHz, CD_2Cl_2 , 298 K): δ 14.21 ($J_{Pt,P} = 3.052 \text{ Hz}$). ¹⁹⁵Pt{¹H} NMR (107 MHz, CD_2Cl_2 , 298 K): δ –4,442.79. Anal. calc. for 1, $C_{142}H_{84}B_2F_{48}Pt_2P_4S_8$: C 48.81%, H 2.42%, N 0%; found: C 48.79%, H 2.94%, N none.

Synthesis of $[\{(PPh_3-d_{15})_2Pt\}_2TTFtt][BAr_4]_2$ (1-d₆₀)

TTFtt(SnBu₂)₂ (0.015 g, 0.018 mmol) was dissolved in 3 mL of DCM and slowly added to a solution of Pt(PPh₃- d_{15})₂Cl₂ (0.030 g, 0.037 mmol) in 3 mL of





DCM. The colorless solution formed a shiny pink suspension upon addition of TTFtt(SnBu₂)₂ and was left to stir for 10 min. Next, [Fc^{BzO}][BAr^F₄] (0.043 g, 0.037 mmol) was dissolved in 3 mL DCM and slowly added to the stirring reaction. The shiny pink suspension turned brown and then green upon full addition of [Fc^{BzO}][BAr^F₄] and was left to stir for 5 min. The solution was condensed to 1 mL under vacuum and petroleum ether (5 mL) was slowly added to further precipitate out the final product. Green crystals formed immediately. The solids were washed with petroleum ether several times (3 x 5 mL) and dried under vacuum. The crude product was redissolved in 1 mL of DCM, filtered through celite, and layered with petroleum ether. The layered solution was cooled to -35° C and left to crystallize overnight. The resulting green crystals were collected and dried (0.060 g, 92% yield). Crystals suitable for diffraction were selected from a dichloromethane/petroleum ether slow diffusion gradient left to crystallize overnight at -35°C. ¹H NMR (500 MHz, CD_2Cl_2 , 298 K): δ 7.55 (s, $[BAr_4^F]^-$), 7.72 (s, $[BAr_4^F]^-$). $^{31}P\{^1H\}$ NMR (162 MHz, CD_2Cl_2 , 298 K): δ 13.75 ($J_{Pt,P}$ = 3,049 Hz). ¹⁹⁵Pt{¹H} NMR (107 MHz, CD_2Cl_2 , 298 K): δ -4,444.89.

SUPPLEMENTAL INFORMATION

Supplemental information can be found online at https://doi.org/10.1016/j.chempr. 2024.03.023.

ACKNOWLEDGMENTS

J.S.A. and D.A.M. gratefully acknowledge support for this work from the U.S. Department of Energy, Office of Science, Office of Basic Energy Sciences, under the grant DE-SC0019215. J.S.A. also gratefully acknowledges support from a Dreyfus Teacher-Scholar Award (TC-21-064). D.A.M. also gratefully acknowledges the U.S. National Science Foundation (NSF) grant no. CHE-2155082. This work was supported by the Chicago MRSEC, which is funded by the NSF through the grant DMR-1420709. This work was performed, in part, at the Soft Matter Characterization Facility at the Pritzker School of Molecular Engineering at the University of Chicago. Part of this work was performed at the Center for Nanoscale Materials, a DOE Office of Science User Facility, and supported by the U.S. Department of Energy, Office of Science, Office of Basic Energy Sciences under contract no. DE-AC02-06CH11357. Philippe Guyot-Sionnest and Ananth Kamath are thanked for helpful discussions.

AUTHOR CONTRIBUTIONS

L.E.M. synthesized the complexes and performed characterization and photophysical measurements. J.-N.B. and D.A.M. performed and interpreted the CASSCF and DFT calculations. C.M. performed PLQY measurements and provided energy gap law analysis. S.W.A. collected and solved the crystallographic data. R.D.S. and L.E.M. performed the TA, VT PL, and TCSPC measurements, and the lasing experiments. L.E.M., C.M., and J.S.A. conceived the project. L.E.M. and J.S.A. wrote the manuscript along with all authors.

DECLARATION OF INTERESTS

L.E.M., R.D.S., and J.S.A. have a patent filed on this work.

Received: December 22, 2023 Revised: February 21, 2024 Accepted: March 25, 2024 Published: April 18, 2024

Chem Article



REFERENCES

- Hong, G., Antaris, A.L., and Dai, H. (2017). Near-Infrared Fluorophores for Biomedical Imaging. Nat. Biol. Eng. 1, 10. https://doi.org/ 10.1038/s41551-016-0010.
- Matsui, A., Tanaka, E., Choi, H.S., Winer, J.H., Kianzad, V., Gioux, S., Laurence, R.G., and Frangioni, J.V. (2010). Real-Time Intra-Operative Near-Infrared Fluorescence Identification of the Extrahepatic Bile Ducts Using Clinically Available Contrast Agents. Surgery 148, 87–95. https://doi.org/10.1016/j. surg.2009.12.004.
- Li, B., Zhao, M., Feng, L., Dou, C., Ding, S., Zhou, G., Lu, L., Zhang, H., Chen, F., Li, X., et al. (2020). Organic NIR-II Molecule with Long Blood Half-Life for in Vivo Dynamic Vascular Imaging. Nat. Commun. 11, 3102. https://doi. org/10.1038/s41467-020-16924-z.
- 4. Qu, C., Xiao, Y., Zhou, H., Ding, B., Li, A., Lin, J., Zeng, X., Chen, H., Qian, K., Zhang, X., et al. (2019). Quaternary Ammonium Salt Based NIR-II Probes for in Vivo Imaging. Adv. Opt. Mater. 7, 1900229. https://doi.org/10.1002/adom. 201900229.
- Zeng, X., Xiao, Y., Lin, J., Li, S., Zhou, H., Nong, J., Xu, G., Wang, H., Xu, F., Wu, J., et al. (2018). Near-Infrared II Dye-Protein Complex for Biomedical Imaging and Imaging-Guided Photothermal Therapy. Adv. Health Mat. 7, e1800589. https://doi.org/10.1002/adhm. 201800589
- Antaris, A.L., Chen, H., Diao, S., Ma, Z., Zhang, Z., Zhu, S., Wang, J., Lozano, A.X., Fan, Q., Chew, L., et al. (2017). A high quantum yield molecule-protein complex fluorophore for near-infrared II imaging. Nat. Commun. 8, 15269. https://doi.org/10.1038/ncomms15269.
- Wu, J.-J., Wang, X.-D., and Liao, L.-S. (2019). Near-Infrared Solid-State Lasers Based on Small Organic Molecules. ACS Photon. 6, 2590–2599. https://doi.org/10.1021/ acsphotonics.9b01187.
- Song, Y., Yu, G., Xie, B., Zhang, K., and Huang, F. (2020). Visible-to-Near-Infrared Organic Photodiodes with Performance Comparable to Commercial Silicon-Based Detectors. Appl. Phys. Lett. 117, 093302. https://doi.org/10. 1063/5.0018274
- Ho, C.-L., Li, H., and Wong, W.-Y. (2014). Red to Near-Infrared Organometallic Phosphorescent Dyes for OLED Applications. J. Organomet. Chem. 751, 261–285. https://doi.org/10.1016/j. jorganchem.2013.09.035.
- Borel, A., Habrant-Claude, T., Rapisarda, F., Reichel, J., Doorn, S.K., Voisin, C., and Chassagneux, Y. (2023). Telecom Band Single-Photon Source Using a Grafted Carbon Nanotube Coupled to a Fiber Fabry-Perot Cavity in the Purcell Regime. ACS Photonics 10, 2839–2845. https://doi.org/10.1021/ acsphotonics.3c00541.
- Antaris, A.L., Chen, H., Cheng, K., Sun, Y., Hong, G., Qu, C., Diao, S., Deng, Z., Hu, X., Zhang, B., et al. (2016). A Small-Molecule Dye for NIR-II Imaging. Nat. Mater. 15, 235–242. https://doi.org/10.1038/nmat4476.
- 12. Zhang, R., Xu, Y., Zhang, Y., Kim, H.S., Sharma, A., Gao, J., Yang, G., Kim, J.S., and Sun, Y.

- (2019). Rational Design of a Multifunctional Molecular Dye for Dual-Modal NIR-II/ Photoacoustic Imaging and Photothermal Therapy. Chem. Sci. 10, 8348–8353. https://doi.org/10.1039/c9sc03504d.
- Sun, C., Li, B., Zhao, M., Wang, S., Lei, Z., Lu, L., Zhang, H., Feng, L., Dou, C., Yin, D., et al. (2019). J-Aggregates of Cyanine Dye for NIR-II in Vivo Dynamic Vascular Imaging Beyond 1500 nm. J. Am. Chem. Soc. 141, 19221–19225. https://doi.org/10.1021/jacs.9b10043.
- Lei, Z., Sun, C., Pei, P., Wang, S., Li, D., Zhang, X., and Zhang, F. (2019). Stable, Wavelength-Tunable Fluorescent Dyes in the NIR-II Region for In-Vivo High-Contrast Bioimaging and Multiplexed Biosensing. Angew. Chem. Int. Ed. Engl. 58, 8166–8171. https://doi.org/10.1002/ anie.201904182.
- Englman, R., and Jortner, J. (1970). The Energy Gap Law for Radiationless Transitions in Large Molecules. Mol. Phys. 18, 145–164. https://doi. org/10.1080/00268977000100171.
- Bixon, M., and Jortner, J. (1968). Intramolecular Radiationless Transitions. J. Chem. Phys. 48, 715–726. https://doi.org/10.1063/1.1668703.
- Kubo, R. (1952). Thermal Ionization of Trapped Electrons. Phys. Rev. 86, 929–937. https://doi. org/10.1103/PhysRev.86.929.
- Lin, S.H., and Bersohn, R. (1968). Effect of Partial Deuteration and Temperature on Triplet-State Lifetimes. J. Chem. Phys. 48, 2732–2736. https://doi.org/10.1063/1.1669507.
- Bixon, M., and Jortner, J. (1969). Electronic Relaxation in Large Molecules. J. Chem. Phys. 50, 4061–4070. https://doi.org/10.1063/1. 1671665.
- Robinson, G.W., and Frosch, R.P. (1962). Theory of Electronic Energy Relaxation in the Solid Phase. J. Chem. Phys. 37, 1962–1973. https:// doi.org/10.1063/1.1733413.
- Robinson, G.W., and Frosch, R.P. (1963). Electronic Excitation Transfer and Relaxation. J. Chem. Phys. 38, 1187–1203. https://doi.org/ 10.1063/1.1733823.
- Friedman, H.C., Cosco, E.D., Atallah, T.L., Jia, S., Sletten, E.M., and Caram, J.R. (2021). Establishing Design Principles for Emissive Organic SWIR Chromophores from Energy Gap Laws. Chem 7, 3359–3376. https://doi.org/ 10.1016/j.chempr.2021.09.001.
- Lin, S.H. (1970). Energy Gap Law and Franck– Condon Factor in Radiationless Transitions.
 J. Chem. Phys. 53, 3766–3767. https://doi.org/ 10.1063/1.1674571.
- Freed, K.F., and Jortner, J. (1970). Multiphonon Processes in the Non-radiative Decay of Large Molecules. J. Chem. Phys. 52, 6272–6291. https://doi.org/10.1063/1.1672938.
- Freed, K.F. (1978). Radiationless transitions in molecules. Acc. Chem. Res. 11, 74–80. https:// doi.org/10.1021/ar50122a004.
- Jang, S.J. (2021). A simple generalization of the energy gap law for non-radiative processes.
 J. Chem. Phys. 155, 164106. https://doi.org/10. 1063/5.0068868.

- Egorov, S.A., and Skinner, J.L. (1995). On the theory of multiphonon relaxation rates in solids. J. Chem. Phys. 103, 1533–1543. https:// doi.org/10.1063/1.469775.
- Kamath, A., Melnychuk, C., and Guyot-Sionnest, P. (2021). Toward Bright Mid-Infrared Emitters: Thick-Shell n-Type HgSe/CdS Nanocrystals. J. Am. Chem. Soc. 143, 19567– 19575. https://doi.org/10.1021/jacs.1c09858.
- Han, P., and Bester, G. (2015). Carrier relaxation in colloidal nanocrystals: Bridging large electronic energy gaps by low-energy vibrations. Phys. Rev. B 91, 085305. https://doi. org/10.1103/PhysRevB.91.085305.
- Kamath, A., Schaller, R.D., and Guyot-Sionnest, P. (2023). Bright Fluorophores in the Second Near-Infrared Window: HgSe/CdSe Quantum Dots. J. Am. Chem. Soc. 145, 10809–10816. https://doi.org/10.1021/jacs.3c02190.
- Egorov, S.A., and Skinner, J.L. (1996). An improved theory of multiphonon relaxation in solids. J. Chem. Phys. 105, 10153–10155. https://doi.org/10.1063/1.472980.
- Egorov, S.A., Rabani, E., and Berne, B.J. (1999). Non-radiative relaxation processes in condensed phases: Quantum versus classical baths. J. Chem. Phys. 110, 5238–5248. https:// doi.org/10.1063/1.478420.
- Grange, T., Ferreira, R., and Bastard, G. (2007). Polaron relaxation in self-assembled quantum dots: Breakdown of the semiclassical model. Phys. Rev. B 76, 241304. https://doi.org/10. 1103/PhysRevB.76.241304.
- Dmitriev, I.A., and Suris, R.A. (2014). Anharmonicity-assisted multiphonon transitions between distant levels in semiconductor quantum dots. Phys. Rev. B 90, 155431. https://doi.org/10.1103/PhysRevB.90. 155431
- Ridley, B.K. (1978). Multiphonon, non-radiative transition rate for electrons in semiconductors and insulators. J. Phys. C: Solid State Phys. 11, 2323–2341. https://doi.org/10.1088/0022-3719/11/11/023.
- Miyakawa, T., and Dexter, D.L. (1970). Phonon Sidebands, Multiphonon Relaxation of Excited States, and Phonon-Assisted Energy Transfer between lons in Solids. Phys. Rev. B 1, 2961– 2969. https://doi.org/10.1103/PhysRevB. 1.2961.
- Reichenauer, F., Wang, C., Förster, C., Boden, P., Ugur, N., Báez-Cruz, R., Kalmbach, J., Carrella, L.M., Rentschler, E., Ramanan, C., et al. (2021). Strongly Red-Emissive Molecular Ruby [Cr(bpmp)z]³⁺ Surpasses [Ru(bpy)₃]²⁺. J. Am. Chem. Soc. 143, 11843–11855. https://doi.org/10.1021/jacs.1c05971.
- Abe, T., Miyazawa, A., Konno, H., and Kawanishi, Y. (2010). Deuteration isotope effect on non-radiative transition of fac-tris (2phenylpyridinato) iridium (III) complexes. Chem. Phys. Lett. 491, 199–202. https://doi. org/10.1016/j.cplett.2010.03.084.
- Van Houten, J., and Watts, R.J. (1975). The Effect of Ligand and Solvent Deuteration on the Excited State Properties of the Tris(2,2'-bipyridyl)ruthenium(II) Ion in Aqueous





- Solution. Evidence for Electron Transfer to Solvent. J. Am. Chem. Soc. 97, 3843–3844. https://doi.org/10.1021/ja00846a062.
- Wang, S.F., Zhou, D.Y., Kuo, K.H., Wang, C.H., Hung, C.M., Yan, J., Liao, L.S., Hung, W.Y., Chi, Y., and Chou, P.T. (2024). Effects of Deuterium Isotopes on Pt (II) Complexes and Their Impact on Organic NIR Emitters. Angew. Chem. Int. Ed. Engl. 63, e202317571. https://doi.org/10. 1002/anie.202317571.
- Ermolaev, V.L. (2016). The Influence of Deuteration of Complex Organic Molecules on Their Fluorescence Quantum Yielda Review.
 Opt. Spectrosc. 121, 567–584. https://doi.org/ 10.1134/S0030400X16100064.
- Li, D.H., and Smith, B.D. (2021). Deuterated Indocyanine Green (ICG) with Extended Aqueous Storage Shelf-Life: Chemical and Clinical Implications. Chemistry 27, 14535– 14542. https://doi.org/10.1002/chem. 202102816.
- Janeková, H., Friedman, H.C., Russo, M., Zyberaj, M., Ahmed, T., Hua, A.S., Sica, A.V., Caram, J.R., and Štacko, P. (2024). Deuteration of heptamethine cyanine dyes enhances their emission efficacy. Chem. Commun. (Camb) 60, 1000–1003. https://doi.org/10.1039/ d3c05153f.
- 44. Ramos, P., Friedman, H., Li, B.Y., Garcia, C., Sletten, E., Caram, J.R., and Jang, S.J. (2024). Nonadiabatic Derivative Couplings through Multiple Franck-Condon Modes Dictate the Energy Gap Law for Near and Short-Wave Infrared Dye Molecules. J. Phys. Chem. Lett. 15, 1802–1810. https://doi.org/10.1021/acs.jpclett. 3c07629
- McNamara, L.E., Boyn, J.N., Melnychuk, C., Anferov, S.W., Mazziotti, D.A., Schaller, R.D., and Anderson, J.S. (2022). Bright, modular, and switchable near-infrared II emission from compact tetrathiafulvalene-based diradicaloid complexes. J. Am. Chem. Soc. 144, 16447– 16455. https://doi.org/10.1021/jacs.2c04976.
- Tummers, Q.R.J.G., Schepers, A., Hamming, J.F., Kievit, J., Frangioni, J.V., van de Velde, C.J.H., and Vahrmeijer, A.L. (2015). Intraoperative Guidance in Parathyroid Surgery Using Near-Infrared Fluorescence Imaging and Low-Dose Methylene Blue. Surgery 158, 1323– 1330. https://doi.org/10.1016/j.surg.2015. 03.027.
- Dado, R.S., McNamara, L.E., Powers-Nash, M., and Anderson, J.S. (2023). Heteroatom substitution for the development of near-IR lumiphores. J. Trends Chem. 5, 581–583. https://doi.org/10.1016/j.trechm.2022.11.004.
- Fawcett, J., Henderson, W., Kemmitt, R.D.W., Russell, D.R., and Upreti, A. (1996). Synthesis and electrospray mass spectrometry of platinum (II) complexes of 5,5-diethylbarbituric acid (Hdebarb); crystal structure of cis-[PtCl(debarb)(PPh₃)₂] · CH₂Cl₂. J. Chem. Soc. Dalton Trans. 9, 1897–1903. https://doi.org/10. 1039/D19960001897.

- McCullough, R.D., and Belot, J.A. (1994). Toward New Magnetic, Electronic, and Optical Materials: Synthesis and Characterization of New Bimetallic Tetrathiafulvalene Tetrathiolate Building Blocks. Chem. Mater. 6, 1396–1403. https://doi.org/10.1021/cm00044a043.
- Xie, J., Boyn, J.N., Filatov, A.S., McNeece, A.J., Mazziotti, D.A., and Anderson, J.S. (2019). Redox, transmetalation, and stacking properties of tetrathiafulvalene-2,3,6,7tetrathiolate bridged tin, nickel, and palladium compounds. Chem. Sci. 11, 1066–1078. https:// doi.org/10.1039/c9sc04381k.
- Boyn, J.N., McNamara, L.E., Anderson, J.S., and Mazziotti, D.A. (2022). Interplay of Electronic and Geometric Structure Tunes Organic Biradical Character in Bimetallic Tetrathiafulvalene Tetrathiolate Complexes. J. Phys. Chem. A 126, 3329–3337. https://doi. org/10.1021/acs.jpca.2c01773.
- El-Sayed, M.A. (1963). Spin-orbit coupling and radiationless processes in nitrogen heterocyclics. J. Chem. Phys. 38, 2834–2838. https://doi.org/10.1063/1.1733610.
- 53. Baba, M. (2011). Intersystem Crossing in the 1 n π^* and 1 $\pi\pi^*$ States. J. Phys. Chem. A 115, 9514–9519. https://doi.org/10.1021/jp111892y.
- de Caro, D., Fraxedas, J., Faulmann, C., Malfant, I., Milon, J., Lamère, J.-F., Collière, V., and Valade, L. (2004). Metallic Thin Films of TTF [Ni(dmit)₂]₂ by Electrodeposition on (001)-Oriented Silicon Substrates. Adv. Mater. 16, 835–838. https://doi.org/10.1002/adma. 200306427.
- Adamo, C., and Barone, V. (1999). Toward reliable density functional methods without adjustable parameters: the PBE0 model. J. Chem. Phys. 110, 6158–6170. https://doi.org/ 10.1063/1.478522.
- Weigend, F., and Ahlrichs, R. (2005). Balanced basis sets of split valence, triple zeta valence and quadruple zeta valence quality for H to Rn: Design and assessment of accuracy. Phys. Chem. Chem. Phys. 7, 3297–3305. https://doi. org/10.1039/b508541a.
- Frisch, M.J., Trucks, G.W., Schlegel, H.B., Scuseria, G.E., Robb, M.A., Cheeseman, J.R., Scalmani, G., Barone, V., Petersson, G.A., Nakatsuji, H., et al. (2016). Gaussian 16, Revision C.01 (Gaussian Incorp.).
- Neese, F., Wennmohs, F., Becker, U., and Riplinger, C. (2020). The ORCA quantum chemistry program package. J. Chem. Phys. 152, 224108. https://doi.org/10.1063/5. 0004608
- Neese, F., Wennmohs, F., Hansen, A., and Becker, U. (2009). Efficient, approximate and parallel Hartree-Fock and hybrid DFT calculations. A "chain-of-spheres" algorithm for the Hartree-Fock exchange. Chem. Phys. 356, 98–109. https://doi.org/10.1016/j. chemphys.2008.10.036.

- Weigend, F. (2006). Accurate Coulomb-fitting basis sets for H to Rn. Phys. Chem. Chem. Phys. 8, 1057–1065. https://doi.org/10.1039/ b515623h.
- Quillard, S., Louam, G., Buisson, J.P., Boyer, M., Lapkowski, M., Pron, A., and Lefrant, S. (1997). Vibrational spectroscopic studies of the isotope effects in polyaniline. Syn Met. 84, 805–806. https://doi.org/10.1016/S0379-6779(96)04155-0.
- Paulus, B.C., Adelman, S.L., Jamula, L.L., and McCusker, J.K. (2020). Leveraging excited-state coherence for synthetic control of ultrafast dynamics. Nature 582, 214–218. https://doi.org/10.1038/s41586-020-2353-2.
- Kopainsky, B., Qiu, P., Kaiser, W., Sens, B., and Drexhage, K.H. (1982). Lifetime, Photostability, and Chemical Structure of IR Heptamethine Cyanine Dyes Absorbing Beyond 1 μm. Appl. Phys. B 29, 15–18. https://doi.org/10.1007/ BF00694363.
- 64. Kranitzky, W., Kopainsky, B., Kaiser, W., Drexhage, K.H., and Reynolds, G.A. (1981). A new infrared laser dye of superior photostability tunable to 1.24 μm with picosecond excitation. Opt. Commun. 36, 149–152. https://doi.org/10.1016/0030-4018(81)90158-9.
- Elsaesser, T., Polland, H.J., Seilmeier, A., and Kaiser, W. (1984). Narrow-Band Infrared Picosecond Pulses Tunable Between 1.2 and 1.4 μm Generated by a Traveling-Wave Dye Laser. IEEE J. Quantum Electron. 20, 191–194. https://doi.org/10.1109/JQE.1984.1072373.
- McNamara, L.E., Zhou, A., Rajh, T., Sun, L., and Anderson, J.S. (2023). Realizing Solution Phase Room Temperature Quantum Coherence in a Tetrathiafulvalene-Based Diradicaloid Complex. Cell Rep. Phys. Sci. 4, 101693. https://doi.org/10.1016/j.xcrp.2023.101693.
- 67. Sheldrick, G.M. (2015). Crystal structure refinement with SHELXL. Acta Crystallogr. C Struct. Chem. 71, 3–8. https://doi.org/10.1107/S2053229614024218.
- Sheldrick, G.M. (2015). SHELXT- integrated space-group and Crystal-structure determination. Acta Crystallogr. A Found. Adv. 71, 3–8. https://doi.org/10.1107/ S2053273314026370.
- Dolomanov, O.V., Bourhis, L.J., Gildea, R.J., Howard, J.A.K., and Puschmann, H. (2009). Olex2: A complete structure solution, refinement and Analysis Program. J. Appl. Crystallogr. 42, 339–341. https://doi.org/10. 1107/S0021889808042726.
- Bain, G.A., and Berry, J.F. (2008). Diamagnetic Corrections and Pascal's constants. J. Chem. Educ. 85, 532. https://doi.org/10.1021/ ed085p532.